Calhoun

Institutional Archive of the Naval Postgraduate School

Calhoun: The NPS Institutional Archive

Faculty and Researcher Publications	Faculty and Researcher Publications Collection

2008

Optimization of a 3.6-THz quantum cascade laser for real-time imaging with a microbolometer focal plane array

Behnken, Barry

SPIE

Optimization of a 3.6-THz Quantum Cascade Laser for Real-Time Imaging with a Microbolometer Focal Plane Array

Barry N. Behnken[*a], Gamani Karunasiri[a], Danielle Chamberlin[b], Peter Robrish[b], Jérôme Faist[c]

[a]Department of Physics, Naval Postgraduate School, 833 Dyer Rd, Monterey, CA, USA 93943;
[b]Agilent Laboratories, 5301 Stevens Creek Blvd, Santa Clara , CA, USA 95051;
[c]Institute of Physics, Université de Neuchatel, Rue A. L. Bréguet 1, CH-2000 Neuchâtel, Switzerland

ABSTRACT

Real-time imaging in the terahertz (THz) spectral range was achieved using a 3.6-THz quantum cascade laser (QCL) and an uncooled, 160x120 pixel microbolometer camera fitted with a picarin lens. Noise equivalent temperature difference of the camera in the 1-5 THz frequency range was calculated to be at least 3 K, confirming the need for external THz illumination when imaging in this frequency regime. After evaluating the effects of various operating parameters on laser performance, the QCL found to perform optimally at 1.9 A in pulsed mode with a 300 kHz repetition rate and 10-20% duty cycle; average output power was approximately 1 mW. Under this scheme, a series of metallic objects were imaged while wrapped in various obscurants. Single-frame and extended video recordings demonstrate strong contrast between metallic materials and those of plastic, cloth, and paper—supporting the viability of this imaging technology in security screening applications. Thermal effects arising from Joule heating of the laser were found to be the dominant issue affecting output power and image quality; these effects were mitigated by limiting laser pulse widths to 670 ns and operating the system under closed-cycle refrigeration at a temperature of 10 K.

Keywords: THz, microbolometer, uncooled, quantum cascade laser, imaging, detection, camera, NETD.

1. INTRODUCTION

Due to its unique spectral characteristics, radiation in the 0.3-10 THz spectral range has gained recent popularity as a new and potentially powerful medium for next-generation imaging technology.[1-5] Equipped with a proper illuminating source and sensor, THz imaging systems are capable of stand-off imaging of concealed objects and of human body tissue—particularly cancerous growths, which can elude x-ray based imaging detection.[4,5] Such detection agility is due to the fact that THz wavelengths are short enough to provide sub-millimeter resolution capability, but are also long enough to penetrate non-metallic materials.[6,7] Additionally, many explosive materials absorb strongly in the THz frequency range, suggesting numerous applications in the stand-off spectroscopic analysis and identification of concealed explosives.[8,9] Due to a dearth of THz-tuned sensors and sources, however, this frequency range has not been fully exploited to date. Currently, most THz imaging systems are based on either antenna-coupled semiconductor detectors or cryogenically cooled bolometers operating in the scan mode. More recently, the potential use of uncooled microbolometer cameras for THz imaging using quantum cascade laser (QCL) sources have been reported.[10-13] In this paper, we report on the successful use of an uncooled microbolometer infrared camera to image radiation produced by a 3.6-THz QCL with an average output power of 1 mW. Single frame and video recordings of the imaging trials are presented.

---

[*]bnbehnke@nps.edu; phone (831) 656-3331; fax (831) 656-2834; http://www.nps.edu

2. IMAGING SYSTEM

2.1 Sensor

The detection system is a commercially-available, uncooled 160x120 pixel microbolometer focal plane array camera (IR-160, Infrared Systems) capable of passive imaging in the 8-12 μm wavelength band. Since much of the 300 K blackbody spectrum lies within this band, the device has a relatively small noise equivalent temperature difference (NETD). This low NETD (less than 100 mK with f/0.8 optics) is the principal reason microbolometer cameras are capable of generating high-quality infrared images.[10] The pixels are constructed, using conventional MEMS techniques, of a composite film of vanadium oxide (VO_x) and silicon nitride (Si_3N_4). The camera has a dynamic range of 66 dB; camera speed is limited by the 10 ms thermal time constant of the individual pixels, which allows operation at TV frame rates (30 Hz). Since the focal plane array of the camera is not optimized for imaging at THz frequencies, sensitivity of the camera in the 1-5 THz band of interest must be separately evaluated to establish whether external illumination is required to operate the device at such frequencies. NETD for the 1-5 THz frequency band can be estimated using the formula:[13,14]

$$\text{NETD} \quad = \quad \frac{6\,c^2\,F_{no}^2}{A\,\varepsilon\,\pi\,T_l\,k\,\varepsilon_t\,\nu_c^3}\;\text{NEP} \tag{1}$$

where NEP is the noise equivalent power of a single pixel, F_{no} is the f-number of the optics used to focus the beam on the focal plane array, A is the area of a single pixel, ε and ε_t are respective emissivities of the membrane material and source, T_l is the transmissivity of the lens, and ν_c is the high frequency cutoff of the THz region (5 THz).

The microbolometer camera used in the present study employs an f/1 lens with $A = 50 \times 50\ \mu m^2$. Assuming the source to be a blackbody, ε_t can be taken to be unity. Within the 8-12 μm wavelength range, ε is approximately 80%.[14] Noise equivalent power can be determined by considering the various sources of noise within the detector. It has been previously well-established that, in microbolometer detectors, the predominant noise source at lower readout bias currents is Johnson's noise.[14] At room temperature, the RMS voltage of this contribution is given by:[15]

$$V_{JN} = \sqrt{4\,k_B\,T\,R\,\Delta f} = 7.0\,\mu V \tag{2}$$

where $R = 10\ k\Omega$ is the equivalent resistance for noise analysis when the microbolometer and 20 kΩ load resistor are each connected in series in the readout circuit.[14] The frequency bandwidth, Δf, is related to the pixel readout time of the FPA and is equal to one-half the product of the imaging frame rate and the total pixel count. For the 30-Hz frame rate at which the FPA's 160x120 pixel array is individually sampled, then, $\Delta f = 0.29$ MHz. A corresponding NEP can be calculated by dividing this noise voltage by the detector's responsivity, $\mathcal{R}_v = 2 \times 10^5$ V/W.[14] NEP for the system is thus found to be about 35 pW.[14]

The NETD of the microbolometer can be estimated using Eqn. 1 and available parameters for the pixel membrane and focusing optics. Picarin, the material used for focusing optics in these experiments, was measured to have a transmissivity of approximately $T_l = 0.60$ at 3.6 THz. The emissivity metric ε, which is directly proportional to the membrane's absorption of incident radiation, has not been well characterized for THz frequencies. However, by using emissivity values found for infrared frequencies, one can obtain an upper-limit of detector performance and, in turn, determine whether external illumination is necessary under even the most liberal of assumptions. Using $\varepsilon = 0.8$, the NETD of the microbolometer was found to be about 3 K.[14] This value, which is more than an order of magnitude larger than the commercially-specified NETD value (0.1 K) of the camera for passive infrared imaging, confirms the need for external illumination when using the microbolometer camera at THz frequencies. It should be emphasized that the estimated NETD of 3 K is based on membrane emissivity at infrared frequencies. NETD could be considerably higher if the emissivity is reduced at THz frequencies.

2.2 THz QCL Characteristics

The QCL used in these experiments, fabricated via molecular beam epitaxy (MBE) on a semi-insulating GaAs substrate, consists of a 200-μm wide and 14-μm thick multiple quantum well (MQW) active region comprised of 120 periods (Fig. 1).[16] To mitigate heating in the active region, the laser was nominally operated at a 300 kHz pulse repetition rate (PRF) and a duty cycle of 10-20%. With an applied current of 1.9 A, the QCL produces about 5 mW peak output power when operated below 20 K; average output power is approximately 1 mW.[17] To accommodate the laser's stringent cooling requirements, the QCL was mounted on a solid copper block (for dissipation of the thermal energy produced through ohmic heating) and operated within a closed-cycle refrigeration chamber at 10 K (Fig 1).
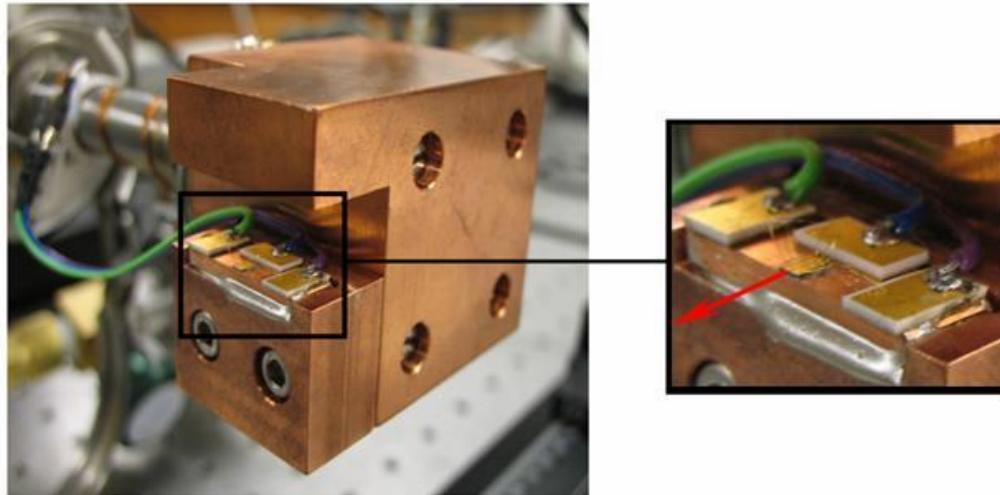

Fig 1. QCL assembly used within cryostat in present study (with external cold head housing removed). Laser element is affixed to a copper carrier to facilitate transfer of thermal energy away from the laser. When lasing, beam is emitted outward, from QCL edge, along direction of red arrow (inset).

Due to the high current and short pulse widths required to drive the QCL, the device was carefully impedance-matched to the 50-Ω pulse generator to ensure efficient transfer of electrical power. This was done by evaluating the QCL's dynamic impedance and designing a step-down transformer with an appropriate number of windings for use in the electrical circuit. Analysis of current-voltage (I-V) data indicates that dynamic impedance of the QCL during operation is approximately 2.7 Ω; as seen in Fig. 2, this result is largely independent of duty cycle. Conversely, insofar as a larger applied voltage is required to produce a given current through the device at higher duty cycles, it is evident that static impedance increases for longer pulse widths. The reasons for this phenomenon have not yet been fully identified; however, it is possible to eliminate the possibility that it is strictly a temperature-driven effect arising from Joule heating. On the contrary, Fig. 3 (I-V data for various cryostat temperatures) clearly demonstrates that static impedance actually *decreases* with increasing cryostat temperature for the particular QCL under investigation. Additional experiments are currently being performed to further investigate the relationship between impedance and duty cycle.
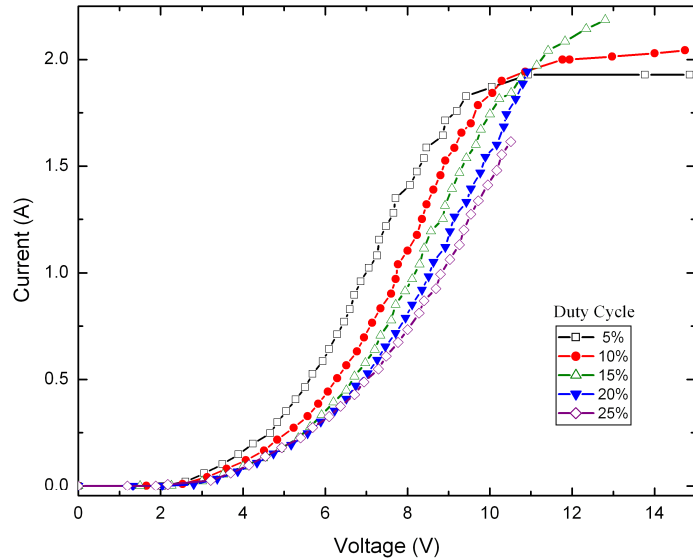
Fig. 2. I-V data for the 3.6-THz QCL, operated under various duty cycles. Dynamic impedance of the device is given by the reciprocal of the slope of the linear region of the curves.
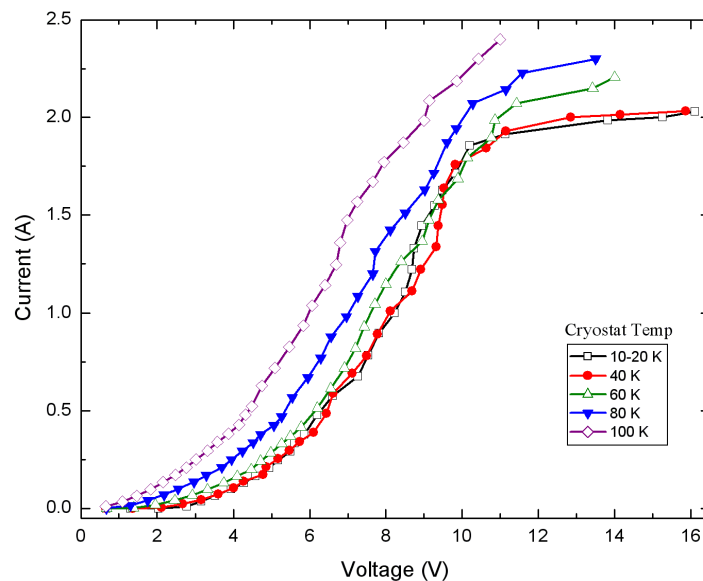

Fig. 3. I-V data of the 3.6-THz QCL, operated under 10% duty cycle, at various cryostat temperatures. The I-V data set labeled as "10-20 K" was collected with cold head thermostat set to 10 K; however, closed-cycle refrigeration was not sufficiently robust to prevent an elevation of temperature (by Joule heating), to as high as 20 K, at higher bias currents.

    Figure 4 shows relative output power of the QCL for a range of applied currents. The laser was operated at duty cycles of 5-25% (170-830 ns pulse length) to determine the optimal pulse conditions for use in imaging experiments. Signal strength was measured by feeding the QCL beam through the external port of a Fourier transform infrared (FTIR) spectrometer and measuring the height of the resulting peak. Each FTIR measurement, consisting of 16 scans, was taken over approximately 35 seconds with an initial cryostat temperature of 10K. Higher duty cycles were found to generally produce higher output power; however, such conditions tend to rapidly warm the laser via Joule heating. With these heating effects was observed a corresponding decline in output power—especially at high applied currents. To the extent that cryostat temperature is unavoidably elevated during QCL operation, then, the results presented in Fig 4 are only representative of *initial* output power from the laser.
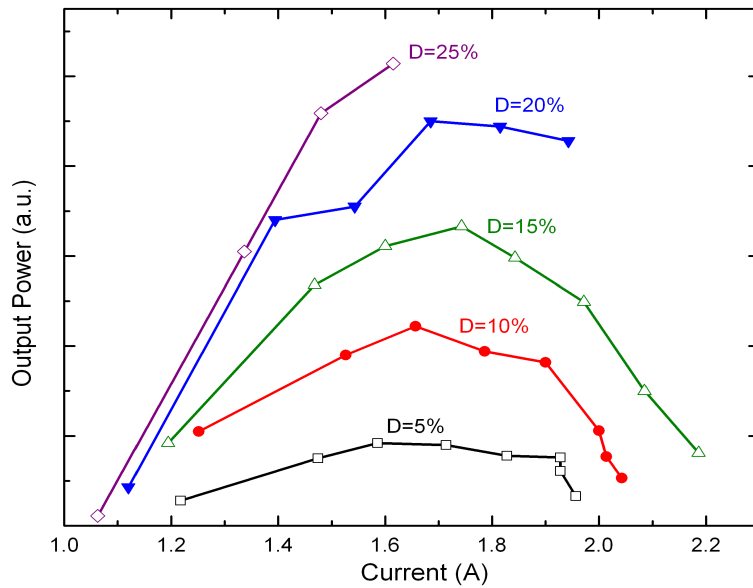
Fig. 4. Output power as a function of current for various duty cycles (D). Each data point was collected by FTIR spectrometry using 16 scans at a resolution of 1 cm^{-1} and a mirror speed of 0.64 m/s.

In contrast, Fig. 5 serves to illustrate QCL performance, at various duty cycles (D), over prolonged periods of time. Although the cryostat thermostat was set to 10 K in each case, close-cycle refrigeration is not sufficiently robust to completely overcome Joule heating of the laser during operation. As a result, temperature of the laser rises until reaching a steady-state value that is dependent upon the applied bias current and selected duty cycle. (For the conditions under which Fig. 5 data were collected, these temperatures were 18 K, 21 K, 24 K, and 32 K for duty cycles of 10%, 15%, 20%, and 25%, respectively).
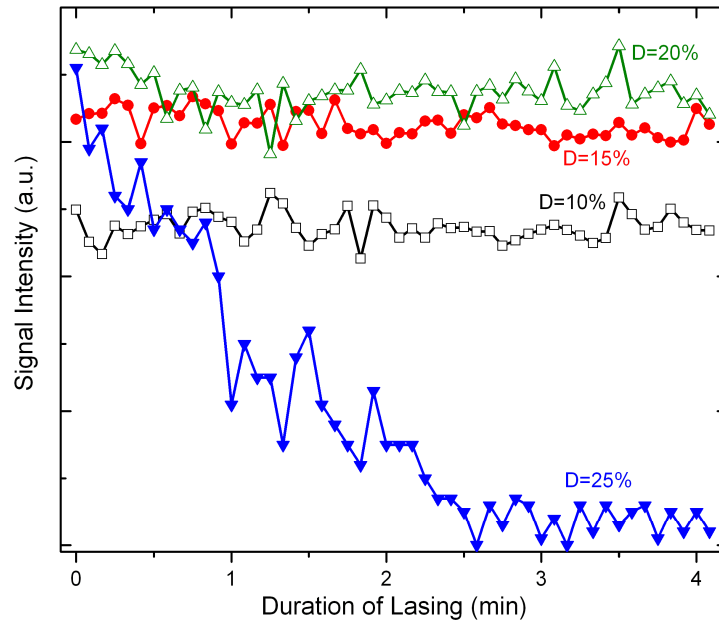

Fig. 5. Effects of temperature on laser performance: Signal intensity detected by FPA while operating QCL, at 300 kHz pulse rate and applied bias of 9.7-10.5 V, over extended period of time. (Cryostat set to 10 K.)

Figure 5 clearly indicates that QCL output at a 25% duty cycle is fundamentally different from that produced at lower duty cycles. Cryostat temperature was found to rise under each scenario. However, whereas signal intensity remains roughly constant in time for duty cycles of 10-20%, it drops precipitously for values above this range. This is likely due to the reduced population inversion that results from thermal excitation of electrons between the quantized energy states of the laser. Driven by these findings, imaging experiments were conducted under different operating conditions, depending upon the type of detection desired. Both still frame images and extended video recordings were performed under more modest operating conditions (typically 1.6-1.9 A, with 15-20% duty cycle.)

In light of these findings, imaging experiments were conducted under different operating conditions, depending upon the type of detection desired. In general, shorter imaging durations allowed for the use of higher quantities of electrical power. For single-frame images taken immediately after the start of lasing, for instance, large voltage bias and high (25%) duty cycle could be successfully used to produce a high-power (albeit short-lived) output beam. In general, though, these aggressive conditions were not found to produce an exceptionally superior output power. Furthermore, due to the lack of imaging persistence they offer, they would have little utility in any practical imaging system. As a result, most imaging—for still frames and extended video recording alike—was performed under more moderate operating conditions (typically 1.6-1.9 A, with 15-20% duty cycle.)

2.3 Image Acquisition

Arrangement of the laser assembly is as shown in Fig. 6. The laser carrier was positioned as close as possible to the edge of the cryostat to maximize transmission of the laser beam through the picarin window. External to the cryostat were placed a pair of gold-plated, 90-degree off-axis parabolic reflectors (f/1 and f/2, each 50.8 mm in diameter) for focusing and steering the beam toward the camera. Initial imaging experiments using the QCL source and off-the-shelf microbolometer camera failed to produce any signal whatsoever. Further examination indicated that this failure was likely not due to a lack of absorption by the pixel membrane layer, but, rather, strong THz attenuation by antireflective coatings applied to the original Ge lens element. To correct this deficiency, the Ge lens was replaced with a 1-inch diameter, 20 mm focal length bi-convex lens made of picarin (PPL-1"-20 mm-BC, Microtech Instruments). Picarin was also used as the source material for the window to the cryostat. At 3.6 THz, the transmittance of the window is about 60%[13]. Imaging experiments were performed by inserting various objects roughly midway between the two parabolic mirrors, which produced a focused image at the microbolometer FPA.
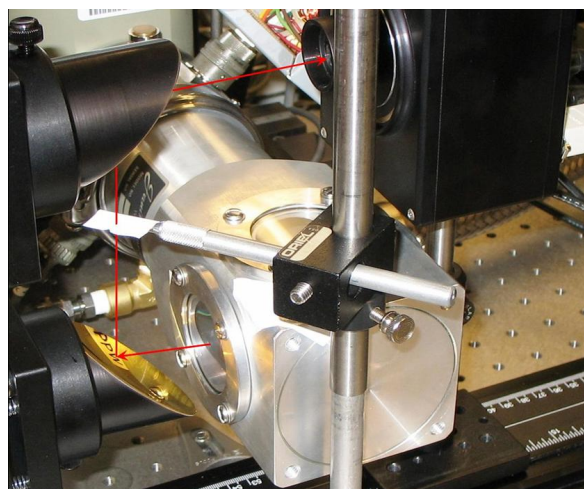

Fig. 6. Optical configuration used for THz imaging. Lower and upper mirrors (50.8 mm and 101.6 mm focal length, respectively) are used to focus and steer the THz beam emerging from the picarin window of the cryostat to the focal plane array of the microbolometer (beam path illustrated by red arrow).

3. RESULTS

Figure 7 is an assembly of images demonstrating the type of real-time imaging that obtainable with the optical arrangement presented above. All images were taken (using framegrabbber software) by the IR-160 microbolometer camera, at a 30-Hz frame rate, under illumination by the aforementioned 3.6-THz QCL. The QCL was operated with a bias of 1.9 A at a 300 kHz pulse rate and 20% duty cycle.
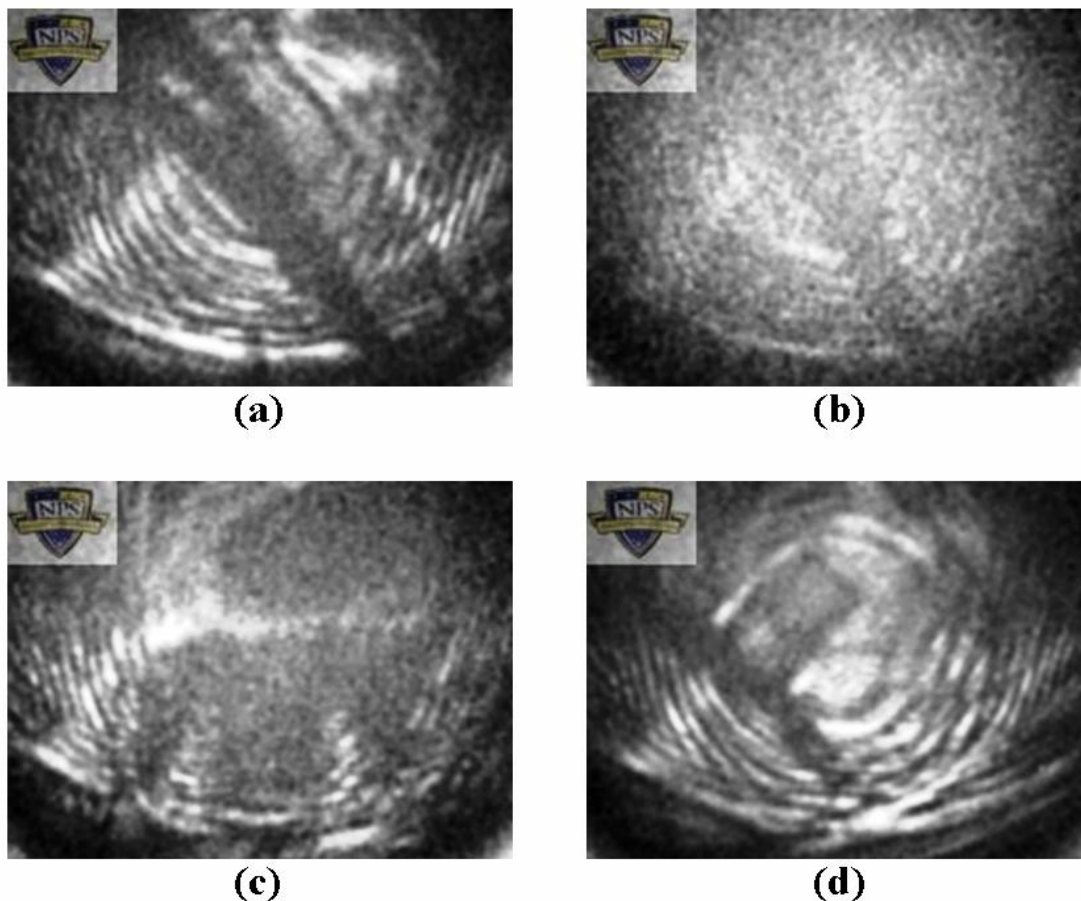

Fig. 7. Still images of video clips from imaging experiments conducted using microbolometer FPA and 3.6-THz QCL operated at a 300 kHz pulse repetition rate, 20% duty cycle, and applied bias of 1.9 A. (a) Steel utility blade obscured by two layers of opaque plastic tape. (b) Utility blade concealed with common bond paper. (c) Mylar[®] film cut in the shape of the Ironman Triathlon[®] "M-Dot" logo and enclosed by two layers of opaque plastic tape. (d) Finger of a black polyurethane glove containing an Allen wrench, which in turn is wrapped with a small swatch of opaque plastic tape.

Interest in THz imaging is largely driven by the fact that, whereas THz radiation is strongly absorbed by metals, it penetrates most non-metallic materials with little-to-no attenuation. This provides exceptional image contrast between metals and obscurants of non-metallic constitution. As is seen in Fig 7, the contrast is particularly striking in the case of plastic materials. Steel blades, such as the one imaged in Fig. 7(a), can be clearly seen when wrapped in opaque plastic tape—and remain visible even when enclosed by as many as eight layers of tape. To a lesser extent, metals are also detectable through cloth and common bond paper (Fig 7(b)). Biaxially-oriented polyethylene terephthalate (boPET) film (more commonly known by the trade name Mylar[®]) was found to also strongly absorb THz radiation—even when used in exceptionally thin quantities (Fig 7(c)). Finally, it is noteworthy that this THz imaging scheme is also capable of imaging non-metallic materials within other non-metallic materials. In Fig 6(d), the THz beam is sufficiently attenuated by both polyethylene and plastic tape that each material can be clearly distinguished from the other.

Given the fact that these imaging results are produced using a rather weak illumination beam (roughly 1 mW), the feasibility of using microbolometers for THz imaging is indeed promising. With a laser source capable of higher power levels, still better image quality should be achievable allowing for imaging through even thicker layers of non-metallic materials.

4. SUMMARY

In summary, we have demonstrated the ability to image metallic objects, obscured by various materials, by using 3.6-THz radiation and a commercially-available microbolometer camera. These results confirm that microbolometer pixel membranes remain absorptive well beyond the 8-12 μm wavelength range, and that uncooled microbolometer cameras hold promise as an inexpensive, compact platform for THz imaging of objects under certain scenarios. Calculations indicate that camera NETD in the 1-5 THz frequency range is at least 3 K, confirming that external radiation sources are necessary in order for such devices to image in the THz regime. For the particular QCL design investigated in this study, a 300 kHz PRF with applied bias of 1.9 A and 20% duty cycle produced optimal laser performance for imaging applications.

ACKNOWLEDGEMENTS

REFERENCES

1. M. B. Campbell and E. J. Heilweil, "Noninvasive detection of weapons of mass destruction using THz radiation," Proc. SPIE 5070, 38 (2003).

2. M. J. Fitch, D. Schauki, C. A. Kelly, and R. Osiander, "Terahertz imaging and spectroscopy for landmine detection," Proc. SPIE 5354, 45 (2004).

3. J. F. Federici, D. Gary, R. Barat, and D. Zimdars, "THz standoff detection and imaging of explosives and weapons," Proc. SPIE 5781, 75-84 (2005).

4. D. A. Zimdars and J. S. White, "Terahertz reflection imaging for package and personnel inspection," Proc. SPIE 5411, 78 (2004).

5. T. Globus, D. Theodorescu, H. Frierson, T. Kchromova, and D. Woolard, "Terahertz spectroscopic characterization of cancer cells," Progress in Biomedical Optics and Imaging 6, 233-240 (2005).

6. J. E. Bjarnason, T. L. J. Chan, A. W. M. Lee, M. A. Celis, and E. R. Brown, "Millimeter-wave, terahertz, and midinfrared transmission through common clothing," Appl. Phys. Lett. 85, 519 (2004).

7. R. H. Clothier and N. Bourne, "Effects of THz exposure on human primary keratinocyte differentiation and viability," J. Biol. Phys. 29, 179–85 (2003).

8. P. Y. Han and X. C. Zhang, "Free-space coherent broadband terahertz time-domain spectroscopy," Meas. Sci. Technol. 12, 1747–1756 (2001).

9. Y. Watanabe, K. Kawase and T. Ikari, "Component spatial pattern analysis of chemicals using terahertz spectral imaging," Appl. Phys. Lett. 83, 800 (2003).

10. G. Karunasiri, "Real time THz camera using microbolometer focal plane array," 7th Int. Conf. on Technol. & the Mine Problem, May 2-4, (2006), Monterey, CA.

11. A. W. M. Lee, and Q. Hu, "Real-time, continuous-wave terahertz imaging by use of a microbolometer focal-plane array," Optics Lett. 30, 2563 (2005).

12. A. W. M. Lee, B. S. Williams, Q. Hu, and J. L. Reno, "Real-time imaging using a 4.3-THz quantum cascade laser and a 320x240 microbolometer focal-plane array," IEEE Photon. Tech. Lett. 18, 1415 (2006).

13. B. N. Behnken, M. Lowe, G. Karunasiri, D. Chamberlin, P. R. Robrish, J. Faist, "Detection of 3.4 THz radiation from a quantum cascade laser using a microbolometer infrared camera," Proc. SPIE 6549, 65490C (2007).

14. R. A. Wood, "Monolithic silicon microbolometer arrays," in Semiconductors and Semimetals 47, 43-121 (1997).

15. E. L. Dereniak and S. D. Boreman, Infrared Detectors and Systems, Wiley, New York, 1996.

16. J. Faist, L. Ajili, G. Scalari, M., Giovannini, M. Beck, M. Rochat, H. Beere, A.G. Davies, E.H. Linfield & D. Ritchie, "Terahertz quantum cascade lasers," Phil. Trans. R. Soc. Lond. 362, 215-231 (2003).

17. D. R. Chamberlin, P. R. Robrish, W. R. Trutna, G. Scalari, M. Giovannini, L. Ajili, and J. Faist, "Imaging at 3.4 THz with a quantum-cascade laser," Appl. Opt. 44, 121-125 (2005).